Journal of Power Sources 613 (2024) 234947

Contents lists available at ScienceDirect

Journal of Power Sources

journal homepage: www.elsevier.com/locate/jpowsour

# Nano-crystalline $Fe_3V_3O_8$ material as an efficient advanced anode for energy storage applications

Rasu Muruganantham [a], Jun-Ying Huang [a], Pei-Jun Wu [a], Liang-Yin Kuo [b,c], Chun-Chuen Yang [d], Yan-Gu Lin [e], Ju Li [f], Wei-Ren Liu [a,*]

[a] Department of Chemical Engineering, R&D Center for Membrane Technology, Center for Circular Economy, Chung Yuan Christian University, 200 Chung Pei Road, Chung Li District, Taoyuan City, 32023, Taiwan
[b] Department of Chemical Engineering, Ming Chi University of Technology, No. 84, Gungjuan Road, Taishan District, New Taipei City, 24330, Taiwan
[c] Center for Sustainability and Energy Technologies, Chang Gung University, Taoyuan City, 33302, Taiwan
[d] Department of Physics, National Central University, Chung-Li District, Taoyuan City-32001, Taiwan
[e] Scientific Research Division, National Synchrotron Radiation Research Center, Hsinchu, 30076, Taiwan
[f] Department of Materials Science and Engineering, Department of Nuclear Science and Engineering, Massachusetts Institute of Technology, Cambridge, MA, 02139, USA

## HIGHLIGHTS

- Nano-sized $Fe_3V_3O_8$ (FVO) cubic crystal phase structure is synthesized by facile hydrothermal route.
- FVO shows excellent high sodium-ion storage capacity as an anode material.
- FVO delivers an initial sodiation capacity of 805 mA h $g^{-1}$ at 100 mA $g^{-1}$.
- FVO sustains a stable capacity of 540 mA h $g^{-1}$ over 200 cycles at 500 mA $g^{-1}$.
- Electrochemical reaction mechanisms for Li/Na-ion storage are predicted.

## GRAPHICAL ABSTRACT

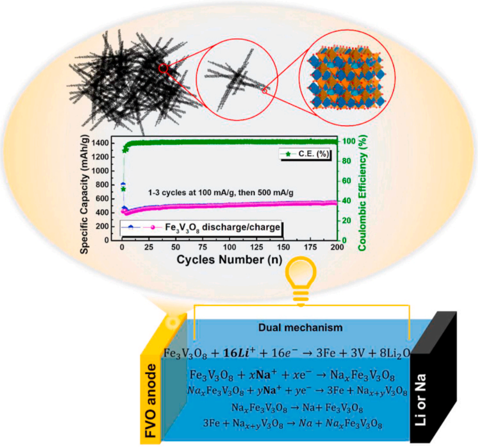

$Fe_3V_3O_8 + \mathbf{16\mathit{Li}^+} + 16e^- \rightarrow 3Fe + 3V + 8Li_2O$

$Fe_3V_3O_8 + x\mathbf{Na}^+ + xe^- \rightarrow Na_xFe_3V_3O_8$

$Na_xFe_3V_3O_8 + y\mathbf{Na}^+ + ye^- \rightarrow 3Fe + Na_{x+y}V_3O_8$

$Na_xFe_3V_3O_8 \rightarrow Na + Fe_3V_3O_8$

$3Fe + Na_{x+y}V_3O_8 \rightarrow Na + Na_xFe_3V_3O_8$

## ARTICLE INFO

*Keywords:*
$Fe_3V_3O_8$
Conversion reaction
Anode
Na-ion battery
Theoretical calculations

## ABSTRACT

The sodium-ion battery (SIB) is a rapidly developing electrochemically rechargeable storage device and a direct substitute for Li-ion batteries. Therefore, identifying novel materials for sodium-ion storage applications is important. Efficient electrodes are particularly desirable for enhancing storage performance in battery applications. In this study, we fabricated a novel $Fe_3V_3O_8$ (FVO) anode material for Na/Li-ion storage using hydrothermal technology for the first time. The electrochemical results indicated that the initial sodiation capacity of the FVO anode is as high as 805 mA h $g^{-1}$ at 100 mA $g^{-1}$, and a reversible sodiation capacity of 540 mA h $g^{-1}$ is maintained over 200 cycles at 500 mA $g^{-1}$, which is more than 1.8 times the commercial hard carbon of ~300

---

* Corresponding author.
*E-mail address:* WRLiu1203@gmail.com (W.-R. Liu).

https://doi.org/10.1016/j.jpowsour.2024.234947
Received 15 February 2024; Received in revised form 18 June 2024; Accepted 19 June 2024

mA h $g^{-1}$. In addition, the oxidation states of the chemical compound and the corresponding sodium reaction mechanism are predicted using X-ray absorption spectroscopy (XAS), X-ray photoelectron spectroscopy (XPS), and *in-situ/ex-situ* X-ray diffraction (XRD) analysis. Overall, the FVO material exhibited significantly higher electrochemical performance, demonstrating promising suitability for sodium-ion storage.

## 1. Introduction

Energy is a hot topic and a key impetus to protect our planet from global warming through the utilization of clean energy technologies. Specifically, the portable and transport sectors urgently require advancements in clean energy storage technology. Thus, batteries represent the utmost potential solution for clean electrical energy storage applications, instead of relying on fossil fuels, which would significantly contribute to a net-zero emissions policy. Nowadays, lithium-ion batteries (LIBs) are widely employed in electric vehicles (EVs), hybrid electric vehicles (HEVs), and portable electronics such as cell phones and laptops because of their merits of energy/power density, lighter weight, no memory effect, and longer cycle life compared to other secondary rechargeable battery systems [1]. However, the Earth's lithium resources are limited, while sodium resources are abundant and cost-effective. Consequently, Na-based batteries, particularly sodium-ion batteries (SIBs), are being considered as promising alternative energy storage devices to replace lithium-based ion storage [2–6]. Nevertheless, SIBs have faced several challenges that have hindered their commercialization, including a larger ionic radius of $Na^+$ (1.02 Å) compared to that of $Li^+$ (0.76 Å), lower energy density and specific capacity. Due to the larger ionic radius issue, it is difficult to use graphite as an anode for high-performance SIBs [7,8]. Therefore, battery scientists are focusing on novel sodium-ion storage anode materials with high-rate and capacity performance for large-scale battery applications.

Anode materials for SIBs can be commonly divided into two categories: carbon-based materials and non-carbon materials. The non-carbon-based pristine transition metal oxides (TMOs) identified as anode materials exhibited higher theoretical capacity and a wider operating potential [9–13]. In general, TMOs can be distinguished into several types, such as mono-oxides ($AO_x$) [14–17], bimetallic oxides [18–24], ternary-metal oxides [25–27] and so on. Among these categories, metal vanadates ($A_xV_yO_z$, A = transition metal such as Co, Ni, Cu, Zn, and so on) have garnered considerable attention as promising electrodes, owing to their multiple valence states and extensive use in Li-ion storage [28–33]. *Jin* et al. [34] synthesized 2D $Zn_3V_3O_8$ microsheets through a combination of the solvothermal method and heat treatment. The as-synthesized $Zn_3V_3O_8$ microsheets without heat treatment delivered an initial Li-ion discharge capacity of 752 mA h $g^{-1}$ at 100 mA $g^{-1}$. Moreover, after heat treatment at 550 °C, the sample cell exhibited an initial discharge capacity of 1152 mA h $g^{-1}$ and retained around 901 mA h $g^{-1}$ after 100 cycles. *Cheng* et al. [8] described a 3D flower-like $Zn_3V_3O_8$ coupled with *N*-doped carbon nanospheres anode synthesized via the microemulsion with calcination approach for Li/Na-ion batteries. The $Zn_3V_3O_8$ nanospheres demonstrated a reversible discharge capacity of around 1141 mA h $g^{-1}$ after 200 cycles for LIBs and 113 mA h $g^{-1}$ after 400 cycles for SIBs at a current density of 200 mA $g^{-1}$. *Nie* et al. [35] proposed the 3D binder-free grass-like $Zn_3V_3O_8$ nanobelts coated carbon fiber cloth ($Zn_3V_3O_8$/CFC) as an anode for LIBs through annealing treatment consisting of a hydrothermal process. The delivered rescindable capacity of ~1750 mA h $g^{-1}$ at a low current density of 100 mA $g^{-1}$ and 942 mA h $g^{-1}$ of specific capacity was observed at the high rate of 1.5 A $g^{-1}$. *Xue* et al. [36] reported successfully lychee-like $Zn_3V_3O_8$@C/rGO composite nanospheres via a one-step ethanol-based thermal reduction technique. The composite $Zn_3V_3O_8$@C/rGO revealed a reversible discharge capacity of 1012 mA h $g^{-1}$ after 200 cycles at a current density of 100 mA $g^{-1}$ and high-rate capability of 448 mA h $g^{-1}$ at 4000 mA $g^{-1}$ over 1000 cycles. *Bie* et al. [37] proposed the hierarchical $Zn_3V_3O_8$@C nanoplates composite anode for LIBs via a simple reverse microemulsion procedure with a consequent annealing method. The $Zn_3V_3O_8$@C composite anode observed a specific discharge capacity of 912 mA h $g^{-1}$ at 0.4 A $g^{-1}$ and exposed good cyclic stability as 756 mA h $g^{-1}$ at 1.6 A $g^{-1}$ after 500 cycles. *Liu* et al. [38] prepared the nitrogen-doped carbon-wrapped $Zn_3V_3O_8$ ($Zn_3V_3O_8$/NC) microspheres composite anode for Li/Na-ion batteries. The $Zn_3V_3O_8$/NC anode delivered initial sodiation/desodiation capacities of 693/302 mA h $g^{-1}$ with a coulombic efficiency of 43.6 %. *Bai* et al. [39] evaluated the electrochemical performance of porous CNTs encapsulated $Zn_3V_3O_8$ as an anode material for LIBs, which possessed an excellent rate capacity of 1013 and 329 mA h $g^{-1}$ at 200 and 8000 mA $g^{-1}$, respectively. Moreover, it was observed appreciable cyclic stability of 470 mA h $g^{-1}$ after 300 cycles at 3000 mA $g^{-1}$.

Transition metal vanadate in sodium ion batteries is limited. Transition metal vanadate's offer several advantages [40]: (i) Due to the multivalent nature of vanadium, they exhibit rich redox chemistry and offer higher capacity. (ii) They have high electrochemical activity. (iii) They have good structural stability. (iv) Resources for the transition metal vanadium (V) are abundant, and the production of its oxides is simple, inexpensive, and environmentally friendly. Therefore, transition metal vanadate's hold great potential as anode materials for sodium ion batteries. Furthermore, nanoscale structures are feasible for suppressing volume changes and reducing ion diffusion pathways, thereby endowing vanadate electrodes with excellent rate capabilities [41]. The $Fe_3V_3O_8$ crystal belongs to the spinel structure. Generally, the chemical formula for oxide spinels can be written as $AB_2O_4$, where A and B represent cations in tetrahedral and octahedral coordination, respectively, with O being the oxygen ion. In the normal spinel structure, the A-site cations occupy 1/8 of the tetrahedral holes, while the B-site cations fill 1/2 of the octahedral holes; in inverse spinels, the positions of the A-site ions and half of the B-site ions are swapped. Thus, inverse spinels are represented by formula $B(AB)O_4$, where the AB ions in parentheses occupy the octahedral sites, and the other B ions are in tetrahedral sites. $Fe_3V_3O_8$ falls into the category of mixed spinels, which are intermediate forms between the normal and inverse spinel structures. Consequently, its crystal structure can also be written as $FeV_2O_4 \cdot Fe\ (VFe)O_4$. Due to the differing patterns of filling and intertwining of the tetrahedral and octahedral voids, adjusting the ratio of $(FeV_2O_4)_x \cdot\ (Fe(VFe)O_4)_{1-x}$ allows for the modification of the porosity and ionic channels within the structure. However, to the best of our knowledge, there is rarely a report on $Fe_3V_3O_8$ material and their electrochemical performance of sodium-ion storage.

Therefore, in this study, we investigate the novel pure-phase (pristine) $Fe_3V_3O_8$ (FVO) material via a facile hydrothermal followed by a calcination treatment technique. It is the first time to scrutinize the electrochemical performance of $Fe_3V_3O_8$ as an anode material for SIBs. The FVO material phase purity, morphological view, and chemical properties were systematically studied. FVO consisted of electrode cells that showed remarkable Na-ion storage cyclic and rate capabilities during the $Na^+$ ion insertion/extraction processes. The sodium ion/lithium ion storage was preticted through constant voltage constant current (CCCV) and constant current (CC) mode program. Furthermore, the Na-ion storage mechanism was predicted through *ex-situ* X-ray diffraction analysis of the various potential stages of charged/discharged cell electrodes and described in detail the mechanism.

## 2. Materials and methods

### 2.1. Preparation of $Fe_3V_3O_8$ materials

The $Fe_3V_3O_8$ with porous nanostructure was synthesized via a facile hydrothermal method. First, 0.234 g ammonium metavanadate ($NH_4VO_3$, 99 %, Alfa Aesar) was dissolved in 60 mL deionized water to acquire the solution. Then, 0.808 g of ferric nitrate ($Fe(NO_3)_3{\cdot}9H_2O$, 98 %, J.T. Baker) was poured into the V-source mixed solution and kept stirred for 1 h. The Fe:V ratio was 1:1. Afterwards, 4 mL hydrogen peroxide ($H_2O_2$, 35 %, Showa) was added to the above-mixed solution under a continuous stirrer for 30 min. Subsequently, the mixture solution was transferred to a 100 mL Teflon-lined stainless steel autoclave and reacted at 200 °C for 24 h. Then, the autoclave was cooled to room temperature naturally. The resultant yellow precipitate was collected after washed with deionized water several times and then it was dried at 80 °C. Finally, the as-prepared precipitate was calcined at 500 °C for 4 h under $H_2/N_2$ gas flow using a tube furnace and it was obtained the final product of $Fe_3V_3O_8$ (FVO) (Scheme 1).

### 2.2. Active electrode preparation and fabrication of sodium-ion coin-cell

The electrochemical performance of the obtained product was measured by using a CR2032 coin cell. The working electrode slurry was composed of 80 wt% active material (FVO), 10 wt% conductive agent (Super-P) and 10 wt% binder of sodium-carboxyl-methyl cellulose (CMC)/styrene-butadiene rubber (SBR), respectively. The appropriate amount of deionized water was used as a solvent. The slurry was coated on the 10 μm thickness of copper (Cu) foil and then dried at 120 °C overnight in a vacuum oven to remove the residual water. The dried electrode was roll-pressed and cut into the circular type with 14 mm of diameter. The active material mass loading was maintained at 1.5 mg $cm^{-2}$ for both Li/Na-ion cells. Glass fiber was used as a separator between the active and reference electrodes. The electrolyte was prepared with 1 M $NaClO_4$ in propylene carbonate (PC) and both mixtures were stirred under the glove box for one day. Sodium foil was used as a reference electrode with a diameter of 14 mm. Finally, coin-cells were assembled as shown in Fig. S1. The material and electrochemical characterization conditions, lithium-ion cell assembly and instrument details were described in the supporting information section.

## 3. Results and discussion

### 3.1. Physico-chemical analyses

The cubic spinel nanocrystallite FVO material was produced by a simple hydrothermal method followed by calcination. The graphic image is shown in Scheme 1. Briefly, the precursor of FVO was prepared by mixing simple binary precursors such as $Fe(NO_3)_3{\cdot}9H_2O$ and $NH_4VO_3$ in a hydrothermal reactor. Subsequently, the nano-scale cubic structure of spinel type FVO was obtained by calcination of the reacted product. Fig. 1 (a) depicts the XRD pattern of the as-synthesized $Fe_3V_3O_8$ (FVO) sample. It can be clearly seen in the diffraction peaks (2θ) located at 18.4°, 30.1°, 35.5°, 37.1°, 43.1°, 53.4°, 56.9°, 62.5°, 70.8° and 73.9°, which is obviously well-matched with the literature of $Zn_3V_3O_8$ cubic crystal phase standard pattern (JCPDS no # 31–1477) structure [42]. The exhibited diffraction peaks were ascribed to the plane of (111), (220), (311), (222), (400), (422), (511), (440), (620) and (533), respectively. There were no impurity peaks in the as-synthesized FVO sample. Furthermore, it was predicted the Rietveld refinement of synchrotron XRD of $Fe_3V_3O_8$ and the result is shown in Fig. 1 (b). The structural refinement was done by the Topas software and the derived crystallographic information file (CIF) is enclosed in supporting data. The refinement-derived crystal, lattice parameters are shown in Table 1. It was observed cubic phase structure ($a = b = c$, $\alpha = \beta = \gamma = 90°$) with a space group of *Fd-3m (227),* the lattice constant of $a = 8.4307(13)$ Å and the volume ($V$) = 599.226 $Å^3$, respectively. The obtained lattice parameter was compared with the literature and the result is shown in Table S1. The Rietveld refinement goodness is defined by the following parameters, such as $R_{wp} = 5.24$ %, $R_p = 3.78$ %, and $\chi^2 = 1.39$. Fig. 1 (c) shows the $Fe_3V_3O_8$ cubic phase crystal structure. The structure entails bilayer stacks ($FeO_6/VO_6$) of octahedra alternating with a single layer of tetrahedra ($VO_4$) in the unit cell of cubic phase structure, which is also like the brownmillerite type ordering of Grenier phase model. Additionally, the crystallite size and microstrain of the FVO were analyzed through the Williamson-Hall (W–H) method. Microstrain is due to imperfections within the crystalline lattice, including vacancies, dislocations, stacking faults, and others. Fig. 1 (d) signifies the FVO sample W–H plot of ($_{total}$ cosθ/Kλ) versus (4 sinθ/Kλ) with linear fit the slopes provide the strain value and the line interception in the y-axis gives inverse crystallite size. The prepared FVO crystallite size was 24.57 nm and the microstrain value was $3.64 \times 10^{-3}$. The resulting small crystallite size with fewer imperfections led to an increase in the Na/Li ions cycle via rapid diffusion, and created more active sites for ion storage in electrochemical analysis.

Fig. 2 (a) shows the SEM image of $Fe_3V_3O_8$. This can be seen in the $Fe_3V_3O_8$ sample, which exhibits a nano-sized rod-shaped morphology with diameters of ~20 μm. Fig. 2 (b-d) show the E-mapping images of Fe, V and O in $Fe_3V_3O_8$. It is visible that elements such as Fe, V, and O were homogeneously distributed on the surface. However, the O image showed a higher concentration than that of V and Fe. Furthermore, Fe and V showed similar concentrations in the E-mapping image, suggesting good agreement between theoretical and experimental predictions of $Fe_3V_3O_8$. Furthermore, the Fe/V composition ratio was tested through ICP-OES analysis. The results showed as nearly 1:1 ratio [Fe is 1.933 and V is 1.696], which was good agreement with the experimental values. Fig. 2 (e) displays the HR-TEM image at lower magnification to view the particle morphology. In the prepared FVO, several nano-scale particles can be seen, which are composed of a rod-like shape. The particle size was in the range of 20–25 nm in each case. Furthermore, Fig. 2 (f) demonstrates the lattice view of the $Fe_3V_3O_8$ HR-TEM image at higher magnification. It revealed a lattice fringe with an interplane spacing of 0.25 nm, which corresponds to the (311) plane of the $Fe_3V_3O_8$ structure. The result of FFT [**inset** in Fig. 2 (f)] showed a *d*-space value of 0.254

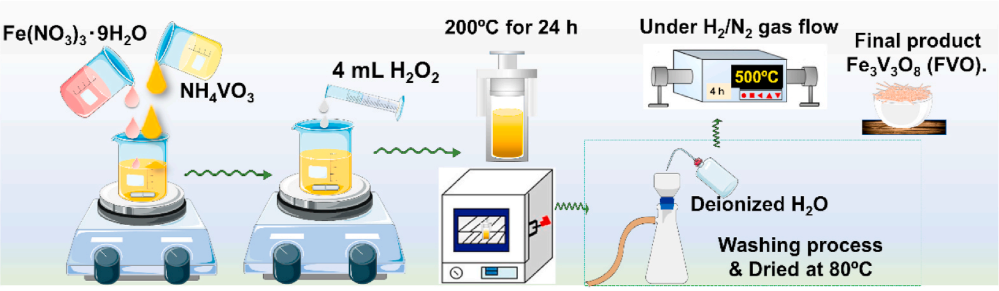

**Scheme 1.** Preparation of $Fe_3V_3O_8$ through hydrothermal one-step heat treatment process.

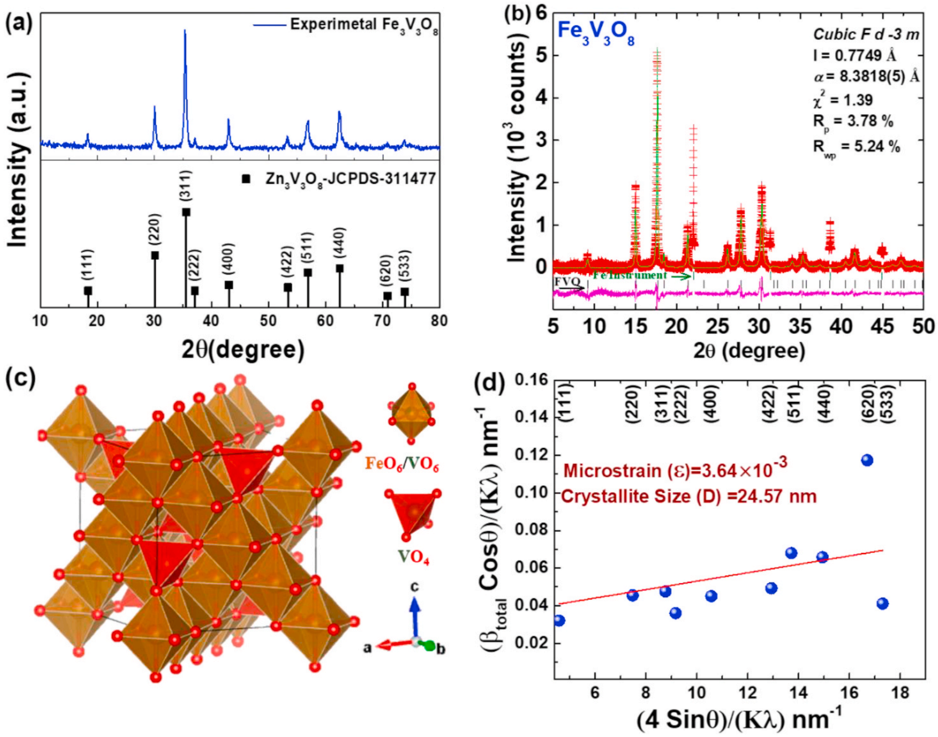

**Fig. 1.** **(a)** XRD pattern of $Fe_3V_3O_8$ with standard pattern of $Zn_3V_3O_8$, **(b)** Rietveld refinement of synchrotron XRD data of $Fe_3V_3O_8$, **(c)** The crystal structures of $Fe_3V_3O_8$ and **(d)** Linear fit plot of Williamson-Hall method (WHM) for calculating crystallite size and microstrain of synthesized $Fe_3V_3O_8$ material.

**Table 1**
Crystal parameters and lattice parameters of $Fe_3V_3O_8$ describing atom positions within the unit cell obtained by Rietveld refinement of the synchrotron XRD pattern.

| $Fe_3V_3O_8$ Cubic *F d -3 m*, a = 8.4307(13) Å | | | | | | |
|---|---|---|---|---|---|---|
| Atoms | *x* | *y* | *z* | Frac | Wyckoff | $U_{iso}$ |
| Fe (1) | 5/8 | 5/8 | 5/8 | 0.875 | 8b | 0.001(1) |
| V (1) | 5/8 | 5/8 | 5/8 | 0.125 | 8b | 0.001(1) |
| Fe (2) | 0 | 0 | 0 | 0.310 | 16c | 0.001(1) |
| V (2) | 0 | 0 | 0 | 0.690 | 16c | 0.001(1) |
| O | 0.2434(4) | 0.2434(4) | 0.2434(4) | 1 | 32e | 0.002(1) |
| $\chi^2 = 1.39$ | | $R_p = 3.78$ % | | $R_{wp} = 5.24$ % | | |

nm, which corresponds to the (311) plane of the $Fe_3V_3O_8$ structure. These results are consistent with the XRD result.

Fig. S2 (a) and **S2 (b)** show the $N_2$ adsorption-desorption isotherm and pore distribution curves of the FVO. It can be seen from the curve of the sample that it belongs to the type IV adsorption-desorption isotherms [43]. This is the feature of mesoporous material. In addition, it can be also seen from the pore size distribution profile that includes micropores and clear visibility of mesopores. Moreover, the mesopore volume is larger than that of the microporous in the $Fe_3V_3O_8$ sample. The observed specific surface area was 20.5 $m^2$ $g^{-1}$ and the mesopore size was in the range of 12–48 nm. Thus, the existing pore structure of the FVO nanocomposite can effectually improve the more active sites by adsorption of Li/Na-ions during the charge/discharge process and increase the specific surface area to promote shorten the diffusion transfer path, which is significant for enlightening the electrochemical performance [44–46].

To further confirm the valence states of the metal in the $Fe_3V_3O_8$ structure, an X-ray photoelectron/absorption spectra (XPS/XAS) were performed. The results are shown in Fig. 3 (a-d). The survey XPS spectrum is shown in Fig. S3. It shows the peaks Fe 2p, V 2p and O 1s, which indicate the presence of Fe, V and O elements in the prepared material. The high-resolution XPS (HR-XPS) spectra of Fe 2*p* are shown in Fig. 3 (a) and show the broad core peaks of Fe $2p_{3/2}$ and Fe $2p_{1/2}$ located at binding energies of 711.0 and 724.3 eV, respectively [44]. Besides, the observed HR-XPS peaks for Fe 2*p* core levels can be divided into $Fe^{2+}$ peaks (Fe $2p_{3/2}$: 710.7 eV, Fe $2p_{1/2}$: 723.75 eV and satellite: 719.2 eV) and $Fe^{3+}$ peaks (Fe $2p_{3/2}$: 712.4 eV, Fe $2p_{1/2}$: 725.4 eV and satellite: 732.67 eV), which may indicate that a mixed valence state of Fe ions was present in the $Fe_3V_3O_8$ sample. The predicted atomic percentage of the Fe ion oxidation state was 74.07 % for $Fe^{2+}$ and 25.93 % for $Fe^{3+}$, retaining the dominant contribution of $Fe^{2+}$ to the formation of the $Fe_3V_3O_8$ structure. Fig. 3 (b) displays the Fe K-edge XAS spectra of $Fe_3V_3O_8$ compared to the reference spectra of Fe, FeO, $Fe_3O_4$ and $Fe_2O_3$, respectively. It can be seen that $Fe_3V_3O_8$ is similar to FeO, which confirms the oxidation state of $Fe^{2+}$. Furthermore, it was slightly coincided with $Fe_2O_3$, resulting in the valence state being $Fe^{2+}$. Therefore, this result showed a mixed oxidation state of iron ($Fe^{2+}/Fe^{3+}$) in the $Fe_3V_3O_8$ structure. Fig. 3 (c) is the V 2p core spectrum which can be distinguished into two parts. The deconvolution of the $V2p_{3/2}$ and $V2p_{1/2}$ peaks exhibits two components corresponding to the $V^{3+}$ and $V^{4+}$ oxidation states, respectively. The binding energies at 516.4 and 523.8 eV are attributed to V $2_{p3/2}$ and V $2_{p1/2}$ of $V^{3+}$, respectively. The peaks at 517.2 and 524.9 eV are ascribed to V $2_{p3/2}$ and V $2_{p1/2}$ of $V^{4+}$, respectively [35,38]. The calculated atomic ratio of $V^{3+}$ to $V^{4+}$ state was 72.93 % and 27.07 %. Meanwhile, by comparing with references V, $V_2O_3$, $VO_2$ and $V_2O_5$, it can be concluded that $Fe_3V_3O_8$ is close to standard $V_2O_3$ and $VO_2$, and confirms that V contained the mixed valences state of $V^{3+}$ and $V^{4+}$ from the V–K-edge XAS spectra of $Fe_3V_3O_8$ [Fig. 3 (d)]. In Fig. 3 (c), there were two peaks in the O 1s core spectrum at 530.2 and 531.4 eV, which are due to the lattice oxygen (metal–oxygen bond) and the hydroxyl oxygen adsorbed on the surface, respectively [35,38]. The mixed valence states of the metals promote electrochemical performance as well as the magnetic applications of spin glass behavior. Therefore, this material can be used for various applications.

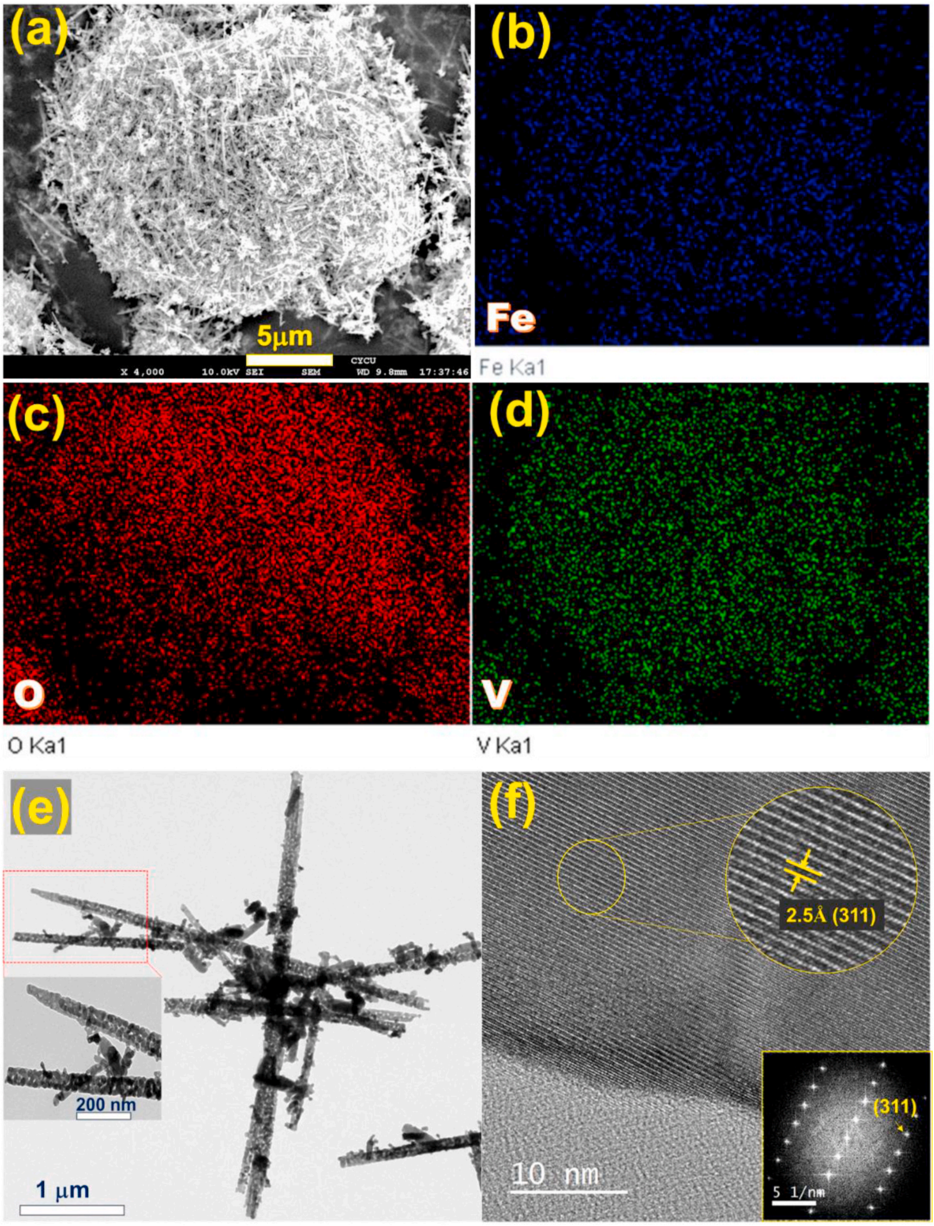

**Fig. 2.** **(a)** SEM image of $Fe_3V_3O_8$, and the presented elemental mapping images of **(b)** Fe **(c)** V **(d)** O, and **(e, f)** Particle morphology image and lattice view of FVO form HR-TEM observation and inset of Fig. 2 (f) is FFT of $Fe_3V_3O_8$.

### 3.2. Theoretical calculations

Density functional theory (DFT) calculations were conducted to investigate the atomic and electronic structures of FVO. A total number of 12 Fe, 12 V and 32-O was employed for the DFT calculations. The results reveal that among the 12 Fe, 7 occupy tetrahedral sites to form $FeO_4$, while 1 V occupies a tetrahedral site, forming $VO_4$. However, 5 Fe and 11 V accommodated the octahedral sites, resulting in the formation of $FeO_6$ and $VO_6$ [Fig. 4 (a)]. The simulated lattice parameters where $a = 8.4474$ Å, $b = 8.3989$ Å, $c = 8.3989$ Å with $\alpha = 89.6358°$, $\beta = 90.1158°$, $\gamma = 90.1158°$ and V = 595.892 Å$^3$ demonstrate agreement with the experimental results shown in Fig. 1 and Table 1. Moreover, to investigate the charge state of Fe and V in FVO, we analyzed the spin density difference (SDD), number of unpair spin electrons (NUE) and density of state (DOS). It is found that all 12 Fe show yellow spherical SDD features in Fig. 4 (b), indicating a higher abundance of up-spin electrons in the orbitals compared to down-spin electrons. The absolute average NUE ($|\overline{\mathrm{NUE}}|$) of 12 Fe is +3.72. The DOS plots, illustrated in Fig. 4 (c), reveal a large occupation of up-spin electrons in both $t_{2g}$ and $e_g$ orbitals. Among them, 8 Fe shows four significant up-spin peaks each occupying the $t_{2g}$ orbitals namely, $d_{xy}$, $d_{yz}$, and $d_{xz}$ as well as the $e_g$ ($d_{z^2}$) orbital, while a major down-spin peak is observed in the $d_{x^2-y^2}$ orbital. Moreover, an up-spin and a single down-spin peak are observed in the $d_{x^2-y^2}$ and $d_{xz}$ orbital above the Fermi level in the DOS plots [Fig. 4 (d-e)], suggesting a possible $Fe^{2+}$ for these 8 Fe. However, 2 out of 12 Fe exhibit a larger number of down-spin electrons below the Fermi level compared to the aforementioned 8 Fe, suggesting a charge state of $Fe^{3+}$ [Fig. S4 (a-b)]. The remaining 2 Fe show an up- and down-spin electron occupation between $Fe^{2+}$ and $Fe^{3+}$ in the DOS plots. This suggests a charge state of $Fe^{(2+\delta)+}$ with $\delta > 0$ for these 2 Fe shown in Fig. S4 (c-d). On the other hand, the yellow and blue SDD features are observed on the 12 V in Fig. 4 (b). The $|\overline{\mathrm{NUE}}|$ value for 7 V is +1.92, while 5 V shows an $|\overline{\mathrm{NUE}}|$ of +0.08. The DOS plots reveal a relative symmetry of up- and down-spin peaks. Among the 12 V ions, 10 show the presence of both up-spin and down-spin electrons in $t_{he\ t2g}$ orbital, suggesting the oxidation of

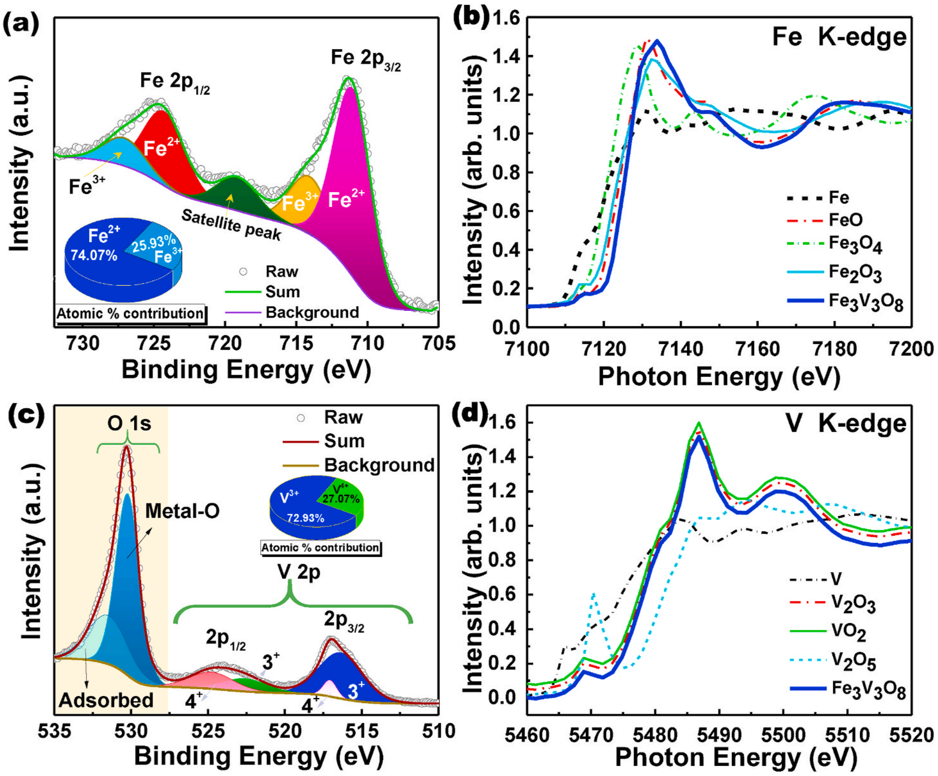

**Fig. 3.** The $Fe_3V_3O_8$ sample: **(a)** high-resolution X-ray photoelectron spectra of Fe 2p, **(b)** X-ray absorption spectra of Fe K-edge with the reference spectra, **(c)** high-resolution X-ray photoelectron spectra of V 2p with O 1s core-level spectra, and **(d)** X-ray absorption spectra of V K-edge with the reference spectra, respectively.

V to $V^{3+}$ [Fig. 4 (f-g)]. However, 2 V exhibits a single down-spin electron in the $t_{2g}$ orbital in the DOS plots, indicating a charge state of $V^{4+}$. In addition to Fe and V, a small variation in SDD features and $|\overline{NUE}|$ value is observed for O ions, indicative of an electron transfer behavior on O [Fig. S4 (e-h)]. Finally, the proposed charge state of 12 Fe and 12 V in FVO are illustrated in Fig. 4 (b).

### 3.3. Evaluation of sodium-ion storage

Fig. 5 (a) shows the cyclic voltammogram (CV) curves of the initial three cycles in the potential window of 0.001–2.5 V *vs.* $Na/Na^+$ under room temperature. In the first cathodic scan, two major reduction (cathodic) peaks can be noticed near 0.5 and 1.0 V, respectively. These cathodic peaks can be ascribed to the intercalation of Na ions into the FVO structure and the conversion of metallic Fe. The reversible cycles (2nd and 3rd) showed shifted peaks with good overlap at 0.84 V and 0.58 V, respectively. This is due to the $Na^+$ insertion of $V_3O_8$-matrix and the formation of metallic Fe. The first CV cycle is different from the subsequent cycles, which is the irreversible cycle from the SEI formation of the first cycle. Meanwhile, the anodic scans showed a peak around 1–2.1 V, which can be caused by the extraction of $Na^+$ from VO-matrix and Na-FVO, respectively. The reversible anodic scans showed good agreement of the currents with the potential, which means good reversibility of the sodium ion insertion/extraction.

The galvanostatic charge-discharge measurements were carried out to evaluate the storage ability of $Fe_3V_3O_8$ (FVO) as an anode for sodium-ion cells through constant voltage constant current (CCCV) and constant current (CC) discharge mode program. The first three cycles were performed at a current density of 100 mA $g^{-1}$ [Fig. 5 (b) and 5 (c)] and the subsequent cycles at 500 mA $g^{-1}$ [Fig. 5 (d)] over 200 cycles of both modes. The FVO electrode exhibits an initial discharge-charge specific capacity of 805 mA h $g^{-1}$ and 420 mA h $g^{-1}$ at 100 mA $g^{-1}$ with the corresponding Coulombic efficiency (ICE) of 52.17 % through the CCCV discharge and CC charge mode. Besides, the CC discharge/charge mode showed a discharge capacity of 588, 332 and 298 mA h $g^{-1}$ for the 1st, 2nd and 3rd cycles with Coulombic efficiency (CE) of 52 %, 85.24 %, 89.60 % respectively. The initial capacity loss is due to the formation of a solid electrolyte interphase (SEI) layer. The observed initial capacity and ICE were higher than in a previous report of a similar metal vanadium oxide ($A_3V_3O_8$, A = transition metal) based anode for sodium-ion batteries [8,38]. Fig. 5 (d) shows the CCCV and CC mode cyclic and coulombic efficiency test of FVO anode. It can be seen in the CCCV test showed a higher reversible specific charge/discharge capacities of 421/465 mA h $g^{-1}$ with coulombic efficiency of 90.59 % in the 2nd cycle and third cycle discharge capacity was observed 454 mA h $g^{-1}$ with the C.E. of 94.49 % at 100 mA $g^{-1}$. Besides, the current density increased to 500 mA $g^{-1}$ and the charge/discharge capacity was 391/426 mA h $g^{-1}$ with an efficiency of 91.79 %. Furthermore, the subsequent cycles showed a slightly increasing behavior of the sodium ion capacity. Meanwhile, the Coulombic efficiency increases rapidly after the activation cycles. The observed discharge capacities were 494, 511, and 533 mA h $g^{-1}$ in the 50th, 100th, and 150th cycles with corresponding efficiencies of 99.24, 99.51 and 99.53 %, respectively. Additionally, the Coulombic efficiency remained at 99.77 % at the stage of 200 cycles at a specific discharge capacity of 540 mA h $g^{-1}$ at 500 mA $g^{-1}$. Moreover, the CC mode test result showed a reversible capacity of 310 mA h $g^{-1}$ at 500 mA $g^{-1}$ over 200 cycles.

Fig. 5 (e) and **5 (f)** show the rate test of charge/discharge profiles of initial cycles through CCCV and CC modes at different current densities from 500 to 1500 mA $g^{-1}$. The rate test was initially carried out 3 cycles at 100 mA $g^{-1}$, for the activation of the electrode cycles and the charge/discharge profile is shown in Fig. S5. The first three cycles showed similar specific capacities to cyclic testing, resulting in good cell reproducibility and stable performance. As shown in Fig. 5 (g) and **5 (h)**, the cyclic rate steadiness test of the FVO anode through CCCV and CC modes. The initial cycle of each current densities reversible specific discharge/charge capacities of FVO at CCCV mode were 419/379, 401/375, 358/334, 318/291, and 253/221 mA h $g^{-1}$ at 500, 800, 1000, 1200

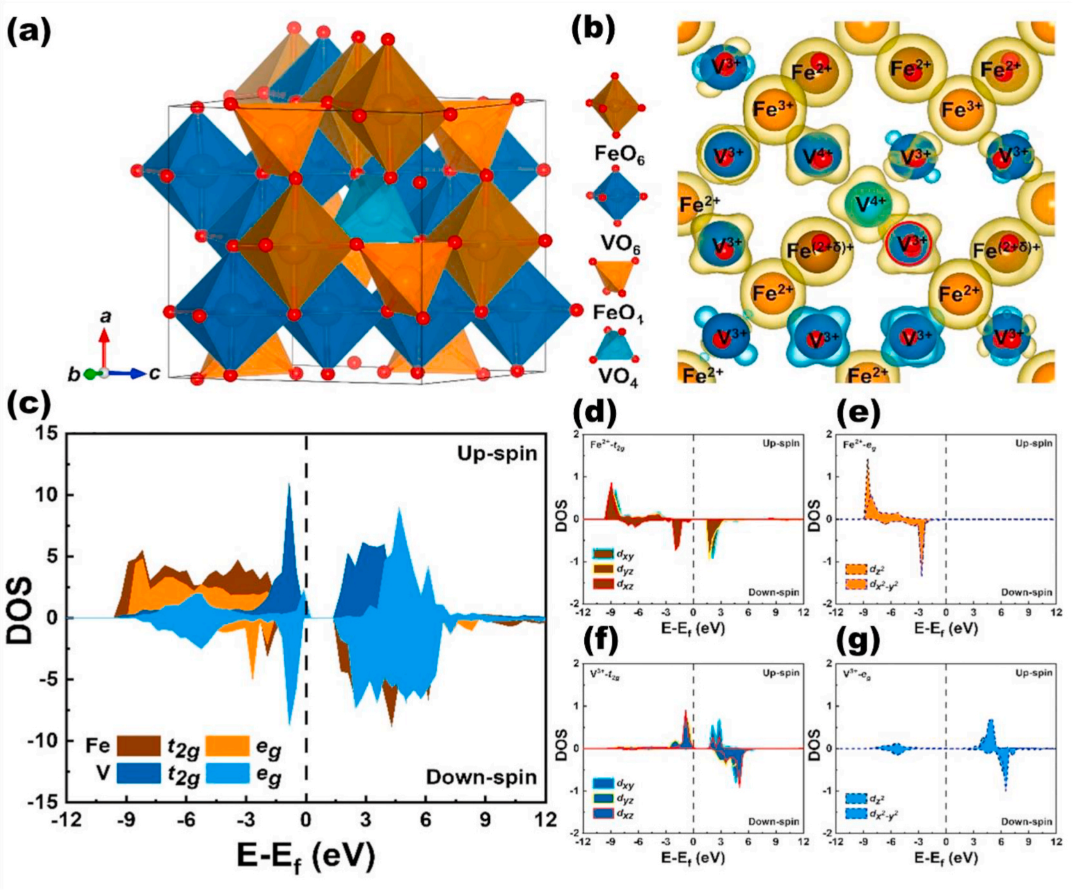

**Fig. 4.** **(a)** Side view of atomic structure of $Fe_3V_3O_8$ (FVO) achieved by a combination of total Coulomb-energy ($E_c$) analysis and density functional theory (DFT) calculation. **(b)** Spin density difference (SDD) and proposed charge state of each Fe and V in FVO. **(c)** Density of state (DOS) of Fe and V in the $t_{2g}$ and $e_g$ orbitals in FVO. **(d–e)** DOS of specified Fe (the Fe on the corner) in three $t_{2g}$ orbitals, namely $d_{xy}$, $d_{yz}$, $d_z$ orbital, and two $e_g$ orbitals, namely $d_{z^2}$ and $d_{x^2-y^2}$ orbital. **(f–g)** DOS of specified V (with red circle) in three $t_{2g}$ orbitals and two $e_g$ orbitals. The yellow and blue features in SDD plots represent up- and down-spin electrons. A SDD isosurface of 0.035 eV/Å$^3$ was used for FVO. (For interpretation of the references to colour in this figure legend, the reader is referred to the Web version of this article.)

and 1500 mA g$^{-1}$, respectively [Fig. 5(g)]. The final cycle (10th) specific discharge/charge capacities were 435/429, 388/384, 348/345, 284/281, and 208/210 mA h g$^{-1}$ at 500, 800, 1000, 1200 and 1500 mA g$^{-1}$, respectively. Conversely, after various higher current densities up to 1500 mA g$^{-1}$, the cell maintained the discharge capacity of 516 mA h g$^{-1}$ at 100 mA g$^{-1}$ over 73 cycles. The results exhibited good rate stability and capacity in the different current densities. Besides, the observed rate performance is better than that of previous reports on similar vanadium oxide-based anode materials for sodium-ion batteries (Fig. S6) [47,48]. Furthermore, the CC mode showed reversible capacities of 219, 180, 144, 128 and 101 mA h g$^{-1}$ at 500, 800, 1000, 1200 and 1500 mA h g$^{-1}$, respectively. The CC mode showed a more stable rate with lesser capacity than that of CCCV discharge mode. Additionally, it tested high rate long-term cyclic capability and the result is shown in Fig. 5 (i). It can be seen in the FVO exposed capacity of 150 mA h g$^{-1}$ at a current density of 2000 mA g$^{-1}$ over 1000 cycles. Furthermore, this suggests that FVO has respectable structural stability and there are more active sites for Na ions in the mesopores, which increases the electrochemical performance. The mesopores can effectively promote the diffusion of electrolyte and migration of Na$^+$, thus maintaining the good performance of the FVO electrode during the (de-) sodiation processes.

Electrochemical impedance spectroscopy (EIS) test was performed to study the kinetic and conductivity behavior of the cells. Fig. 6 **(a)** illustrates the typical Nyquist plots of the cells composed of FVO electrodes before cycles (fresh) and after 200 cycles. The EIS-matched equivalent circuit is shown as an inset in Fig. 6(a). The equivalent circuit consisted of R$_s$ (ohmic resistance), R$_{SEI}$ (SEI film resistance), R$_{ct}$ (charge-transfer resistance), CPE1/CPE2 (double-layer capacitance behavior) and W (Warburg impedance), respectively. The lowest value of contact resistance (Rs) was 5 Ω (at the stage of fresh and after cycles of FVO electrode cells). The fresh cell showed a charge transfer resistance of 4 Ω. However, this increased slightly to 8 Ω after 200 cycles. Furthermore, the R$_{SEI}$ resistance was 71 Ω for fresh cells and 96 Ω for cycling cells. This means that the SEI film formation accelerated after 200 cycles. In addition, the lowest charge transfer resistance can be attributed to the positive effect of Na-ion storage, so the specific capacity is more stable over 200 cycles. However, the formation of SEI could hinder the diffusion of Na-ions in the solid phase. Fig. 6 **(b)** displays the correlation between Z$_{re}$ and ω$^{-1/2}$. It can be seen that the real component of the impedance (Z$_{re}$) has a linear interaction with the reciprocal square root of the angular frequency (ω$^{-1/2}$). The slope values are inversely proportional to the diffusion coefficient of the sodium ions.

### 3.4. *Evaluation of lithium-ion storage*

The Li-ion storage and properties were evaluated using FVO as the anode material of the CR2032 cell, and the results are shown in Fig. 7 (a-f). The oxidation/reduction behavior of the FVO electrode was explored using the cyclic voltammetry (CV) curves in the potential window of 0.001 and 3.5 V *vs.* Li/Li$^+$ at a sweep rate of 0.1 mV s$^{-1}$, as shown in Fig. 7 (a). In the initial cycle, three reduction peaks appear at 1.89 V,

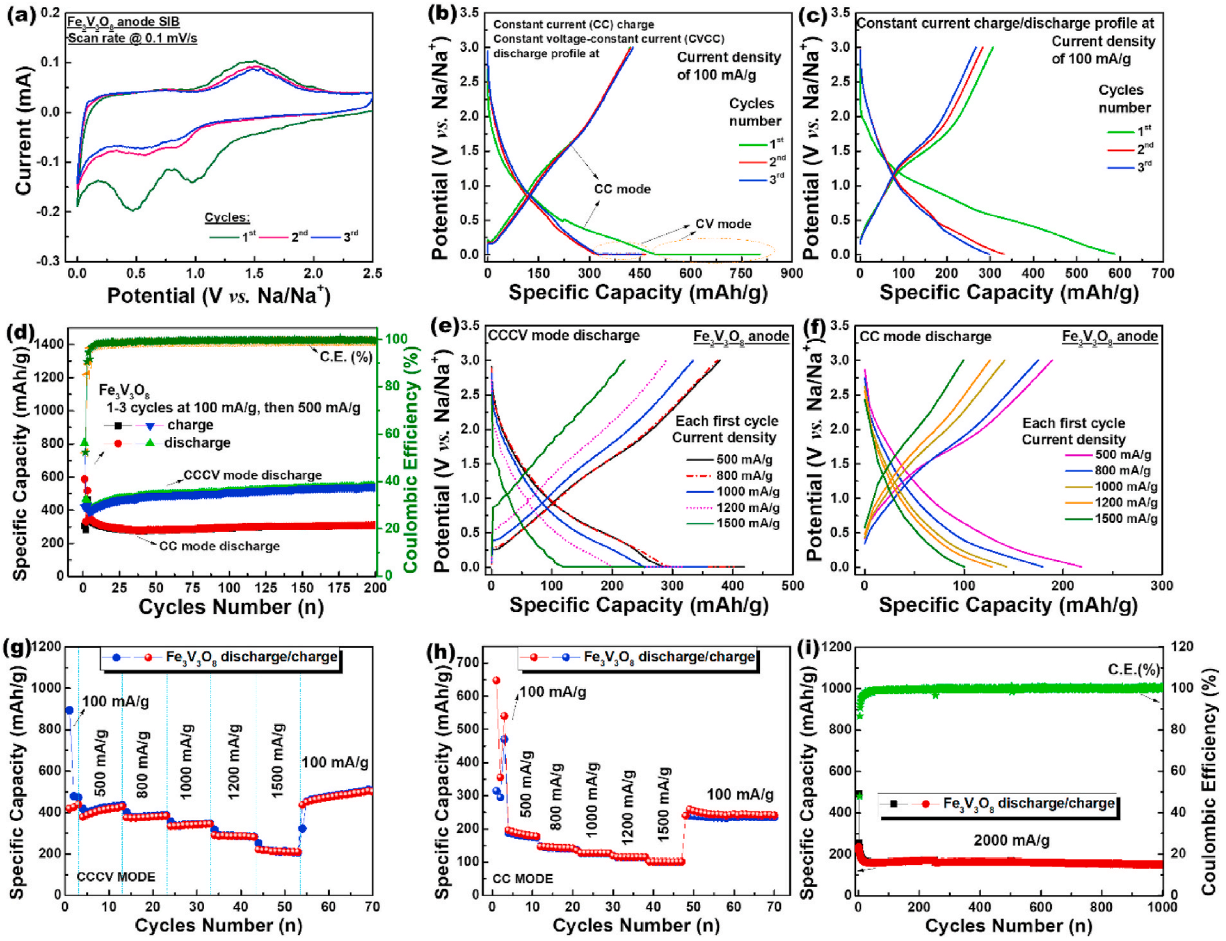

**Fig. 5.** Sodium-ion storage performance using $Fe_3V_3O_8$ (FVO) as anode material: **(a)** cyclic voltammogram (CV), **(b, c)** the galvanostatic charge-discharge profiles of first three cycles at 100 mA $g^{-1}$ through CCCV discharge and CC discharge mode, **(d)** the corresponding cyclic perfromance test, **(e, f)** charge/discharge profiles of initial cycles of different current density at CCCV and CC mode tests, **(g, h)** the corresponding cyclic rate capability of CCCV and CC mode, and **(d)** long-term high current density cyclic test over 1000 cycles at 2000 mA $g^{-1}$.

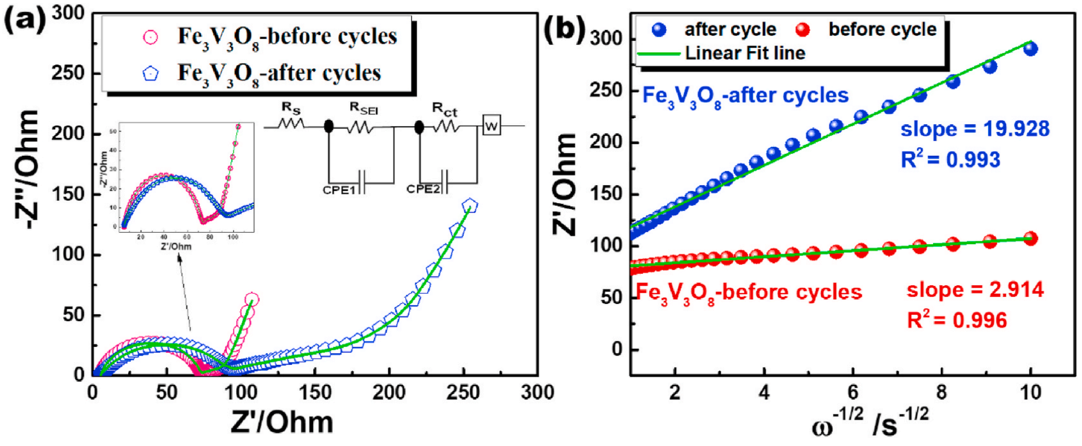

**Fig. 6.** **(a)** Electrochemical impedance spectra before and after $Na^+$ 200 cycles and **(b)** variations and fittings between Z′ and reciprocal square root of the angular frequency ω in the low frequency region.

0.66 V and 0.22 V, which are due to the combined multi-step reaction of FVO such as insertion of lithium ions and conversion of FVO, metal reduction of $Fe^{2+/3+}$ and $V^{3+/4+}$, lithiation of vanadium oxide and the irreversible growth of the solid electrolyte interface layer (SEI) [49]. It can be seen that the peak intensity of the initial scan was reduced in the second and third cycles, leading to the appearance of an irreversible reaction of the electrode (SEI). Besides, the oxidation peaks were found at 1.33 V, 2.09 V and 2.47 V, which can be assigned to the reversible multistep oxidation of Fe, V and the de-lithiation of vanadium oxide [50]. After the initial cycle, the subsequent two cycles are almost overlapped, which reveals a good reversibility during the (de)lithiation cycle process.

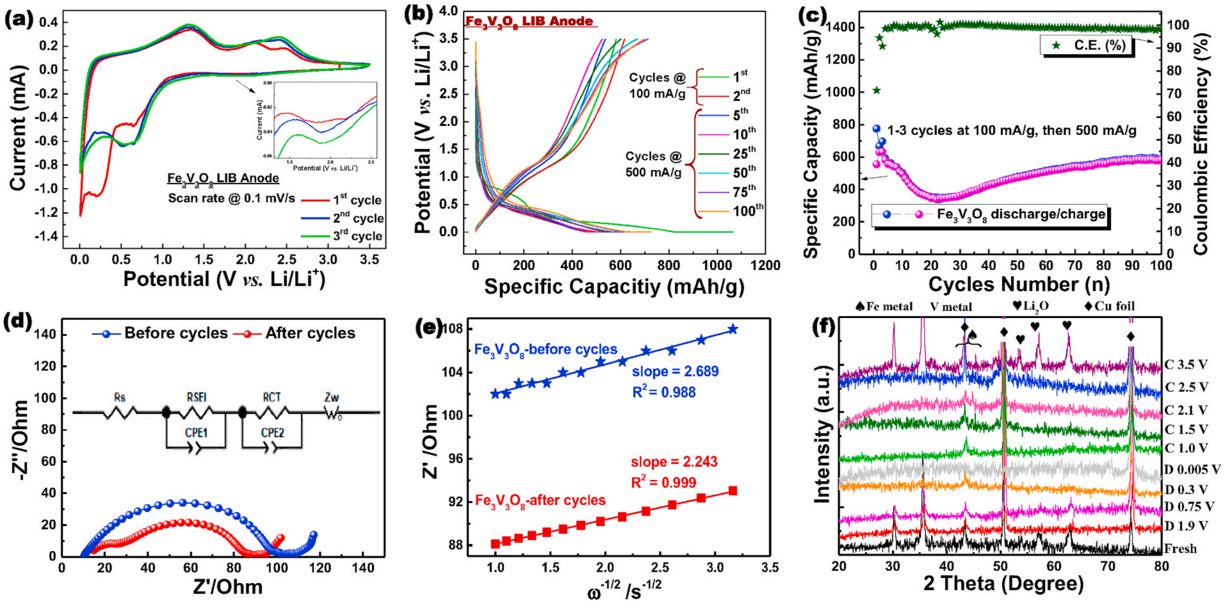

**Fig. 7.** **(a)** The first three CVs cycles for the $Fe_3V_3O_8$ electrode at a scan rate of 0.1 mV s$^{-1}$ in the potential range of 0.001–3.5 V; **(b)** the charge/discharge profiles of selected cycles; **(c)** the corresponding cyclic stability test; **(d)** Electrochemical impedance spectra (EIS) of the $Fe_3V_3O_8$ electrode before and after 100 cycles; **(e)** Linear fitting of the Warburg impedance of the $Fe_3V_3O_8$ electrode and **(f)** *ex-situ* XRD pattern of FVO with different potential points.

Fig. 7 (b) shows the galvanostatic charge-discharge profiles of the FVO anode Li-ion storage capability test in the first two cycles at the current density of 100 mA g$^{-1}$ and the subsequent cycles at 500 mA g$^{-1}$ in the potential window of 0.001–3.5 V. The initial specific discharge/charge capacities were 1066/582 mA h g$^{-1}$ with a Coulombic efficiency (CE) of 54.60 % at 100 mA g$^{-1}$. The low initial CE can be attributed to the initial conversion process (decomposition) of FVO and the formation of the irreversible amorphous Li oxides, the SEI layer, and the decomposition of the electrolyte [49]. However, a reversible discharge capacity of 659 mA h g$^{-1}$ was observed in the second cycle with an increased Coulombic efficiency of about 93.63 %. Fig. 7(c) shows the corresponding cyclic test over 100 cycles with coulombic efficiency. The initial 3 cycles were carried out at 100 mA g$^{-1}$ and the subsequent cycles at 500 mA g$^{-1}$, respectively. It can be seen that a gradually decreasing behavior of the capacities was observed in the first 20 cycles and then an increasing behavior occurred over 80 cycles, which then looks like a stable cyclic behavior over 100 cycles. The similar phenomenon has been observed in the literature of conversion-based transition-metal oxide anode materials for LIBs. This spectacle can be explained as the capacity decay from the activation process, initial phase changes of FVO irreversible processes on the surface of electrodes and the increasing behavior may be due to the reversible progress of polymeric gel-like film, porous morphology, nano-size of particles and interfacial storage of Li ions [49,51–55]. The reversible discharge capacities were 560, 537, 596, 672, 657 mA h g$^{-1}$ and 726 mA h g$^{-1}$ for the 5th, 10th, 25th, 50th, 75th and 100th cycles at a current density of 500 mA g$^{-1}$. The cyclic reversible discharge capacity is proven to be higher than that of similar metal oxide anode materials for LIBs (Table S1) [56].

To investigate the kinetics at the electrode/electrolyte interface of the FVO negative electrode for LIB, the electrochemical impedance spectra (EIS) were performed before and after 100 cycles [Fig. 7 (d)]. The EIS curves consist of a semicircle in the high frequency range and an inclined line in the low frequency range. It can be characterized that the initial region is the formation of a solid electrolyte interface film and/or the contact resistance, and then the intermediate frequency in the semicircle is related to the charge transfer resistance ($R_{ct}$), respectively. Finally, the low-frequency inclined line is called the Warburg impedance ($Z_W$), which characterizes the lithium ion diffusion process. The equivalent circuit diagram is used to analyze the impedance data and the presented diagram is shown in the inset in Fig. 7(d). The EIS resistance and Li-ion diffusion coefficient values derived from the equivalent circuit are listed in Table S2. It can be seen on the FVO electrode, which after 100 cycles showed $R_s$, $R_{ct}$ and $R_{SEI}$ values of 15.27 Ω, 57.54 Ω and 12.69 Ω, respectively. Furthermore, the FVO before cycles showed 12.25 Ω, 65.82 Ω and 18.79 Ω, for $R_s$, $R_{ct}$ and $R_{SEI}$, respectively. Fig. 7 (e) shows the linear fitting of the Warburg impedance of the $Fe_3V_3O_8$ electrode. The estimated Li-ion diffusion coefficients (D) values were $5.05 \times 10^{-13}$ cm$^2$ s$^{-1}$ and $7.26 \times 10^{-13}$ cm$^2$ s$^{-1}$ before and after 100 cycles, which is a higher order than that of binary transition metal mixed oxide anode for LIB's [44,57]. Thus, the sharp slope of the inclined line in the low frequency region indicates the more active lithium ion diffusion, which is in good agreement with the increased charge/discharge capacity resulting from the gradually increasing lithiation during the cycling test.

### *3.5. Analysis of the electrochemical reaction mechanism of Li/Na ions in the Fe3V3O8 anode*

To further explain the electrochemical reaction mechanism and internal structural changes of FVO electrode material during the reaction process in LIBs, *ex-situ* XRD was performed during the discharge phase (from open-circuit voltage to 0.005 V) and charge phase (0.01–3.5 V), as shown in Fig. 7 (f). At the OCV stage, the visible diffraction (2θ) peaks of the FVO electrode were 30.3°, 35.5°, 43.4°, 50.4°, 57.0°, 63.1° and 74.3°, respectively. The diffraction peaks of 43.4°, 50.4° and 74.3° were attributed to the Cu metal from the Cu-foil on the electrode material (Cu, JCPDS No. 04–0836). The diffraction peaks of 30.3°, 35.5°, 43.4°, 57.0° and 63.1° were represented $Fe_3V_3O_8$ cubic crystal phase ($Zn_3V_3O_8$, JCPDS No. 31–1477). Besides, the diffraction peaks were 30.1° and 35.5° owing to the (220) and (311) planes of $Fe_3O_4$ [58]. Additionally, the peaks 36.0°, 44.3° and 64.1° can be attributed to the $Fe_3C$ and Fe metallic, which can be confirmed from the standard data of $Fe_3C$ (JCPDS No. 35–0772) and Fe (JCPDS No. 06–0696) [59,60]. The $Li_2O$ diffraction peaks exposed around 34.0°, 56.0° and 67.0°, which can be confirmed from the $Li_2O$, JCPDS No. 12–0254 [60,61]. Overall, the diffraction peaks in the fully discharged state are amorphous and have lower diffraction intensity, which may be due to the formation of an amorphous SEI layer on the electrode. However, the formation of $Li_2O$

from the diffraction peaks around 54.1°, 56.8° and 62.0° in the fully charged state can be confirmed. Furthermore, the distinct intensity peaks of 30.1° and 35.5° are due to the oxidation of Fe ions. Conversely, the small diffraction peaks around 44–45° were observed due to the metallic Fe, which can be explained that Fe does not completely oxidize, resulting in an initial capacity loss. Sridhar et al. [62] recently reported vanadium dioxide ($VO_2$) powder sample that exhibited peaks at 2θ of 12.2°, 18.3°, 24.1°, 28.4°, 35.9°, 40.2°, 46.1°, and 51.0° (JCPDS No. 31–1438) and Li inserted $V_3O_8$ disclosed peaks at 2θ of 12.0°, 26.2°, 29.4°, 30.2°, 39.2°, 40.5°, 51.4°, 57.9°, and 66.2° (JCPDS No. 73–8166). Therefore, the superimposed diffraction peaks of the Fe–O and V–O oxides make it difficult to clearly distinguish phases. Consistently, the formation of a metallic V or V-matrix can be amorphous and endure the absence of the diffraction peaks. Therefore, the reaction mechanism of bimetal oxide-based materials for use in battery electrodes is eagerly anticipated in the future. Xue et al. [36] proposed the reaction mechanism of $Zn_3V_3O_8$ for LIB anode through CV. The proposed $Zn_3V_3O_8$ decomposed into VO and ZnO, then the VO matrix involved the intercalation of Li and ZnO, further reduced the Zn metal, and then followed the LiZn alloying reaction. Cheng et al. [8] similarly described the reaction mechanism of $Zn_3V_3O_8$ via CV. They described the $Zn_3V_3O_8$ anode to form as an amorphous $Li_yVO_x$ matrix and ZnO, the reduction of $Zn^{2+}$ to Zn, and further the formation of $Li_xZn$. In this case, it is difficult to form a LiFe alloy reaction, so only metallic Fe was formed from the metal oxide. Zhao et al. [50] reported the $Fe_2VO_4$ anode for LIB. The $Fe_2VO_4$ was converted into FeO and $Li_xVO_2$ and then FeO and $Li_xVO_2$ were further lithiated to form the metallic Fe and additional lithiation into the $Li_xVO_2$ matrix. Thus, the reversible capacity was observed from conversion with a combination of intercalation/deintercalation processes.

Based on CV, *ex-situ* XRD and similar structure of the previous reports, the possible reaction mechanism of the FVO material as an anode for LIBs can be expressed as follows.

### 3.5.1. Model:1

Irreversible possible reactions are:

$$Fe_3V_3O_8 + 4Li^+ + 4e^- \rightarrow 3FeO + 3VO + 2Li_2O \tag{1}$$

Reversible reactions are (double conversion reactions):

$$3FeO + 6Li^+ + 6e^- \leftrightarrow 3Fe + 3Li_2O \tag{2}$$

$$3VO + 6Li^+ + 6e^- \leftrightarrow 3V + 3Li_2O \tag{3}$$

(or)

$$VO_x + xLi^+ + xe^- \leftrightarrow Li_xVO_x \tag{4}$$

Overall the reaction is:

$$Fe_3V_3O_8 + 16Li^+ + 16e^- \rightarrow 3Fe + 3V + 8Li_2O \tag{5}$$

### 3.5.2. Model:2

Irreversible possible reactions:

$$Fe_3V_3O_8 + Li^+ + e^- \rightarrow 3FeO + LiV_3O_8 \tag{6}$$

Reversible reactions are (conversion-intercalation reactions):

$$3FeO + 6Li^+ + 6e^- \leftrightarrow 3Fe + 3Li_2O \tag{7}$$

$$LiV_3O_8 + xLi^+ + xe^- \leftrightarrow Li_{1+x}V_3O_8 \tag{8}$$

Based on the lithium ion storage discharge capacity of 1066 mAh $g^{-1}$ the response of Equation (5) [model 1] and the theoretical capacity of 956.44 mA h $g^{-1}$ ($Fe_3V_3O_8$, $M_w = 448.35$ g $mol^{-1}$) can be confirmed. The initial capacity fluctuation compared to the theoretical capacity may indicate the emergence of a positive effect of SEI. Besides, the reversible capacity is based on the conversion reaction of FeO to Fe metallic formation [equation (2)] and intercalation/deintercalation or conversion of VO-matrix [equation (3) or (4)] during the (de)lithiation process.

Fig. 8 (a) shows the ex-situ XRD patterns of the initial sodiation-desodiation process at different potential points at a current density of 100 mA $g^{-1}$. The in-situ XRD patterns view and 2D view with the corresponding discharge/charge profiles of the initial two cycles are shown in Fig. 8 (b-d). The enlargement of the FVO 2θ range is shown in Fig. 8 (e-j). It can be seen that the diffraction peaks differ significantly from those of the LIBs. The discharge state of LIB showed an amorphous diffraction pattern. However, the SIB test at the complete discharge state exposed reduced intensity peaks with slightly shifted diffraction peaks. This phenomenon may be due to the intercalation of sodium-ion, because of the heavier mass and slower mobility of $Na^+$ than $Li^+$ [63], resulting in different phase changes in the $Fe_3V_3O_8$ material during the charge/discharge process. Based on the CV can be identified the oxidation/reduction of the materials showed an intercalation and conversion reaction during the sodium ion storage cycles. The *ex-situ* XRD showed the diffraction peaks of the complete charged state as 21.8°, 26.0°, 30.1°, 34.3°, 35.7°, 37.1°, 40.7°, 43.2°, 45.3°, 47.0°, 49.4°, 51.9°, 53.5°, 57.0°, 58.0° and 62.7° respectively, which is a similar structure of FVO. The peaks were located at around 50.4° and 74.6° corresponding to the Cu-foil of the electrode (Cu, JCPDS No. 04–0836). The observed peaks are a similar plane of the pristine electrode. Moreover, the peaks are slightly shifted to lower and higher angles during the discharge/charge states, which confirms the intercalation reaction. However, the metallic Fe may be amorphous or an obstacle to the electrolyte decomposition (SEI formation). The monoclinic crystalline-like $NaV_3O_8$ phase (space group $P2_1/m$, JCPDS card 45–0498) showed very small intensity diffraction peaks than that of cubic FVO structure. Besides, It can be seen in the original FVO diffraction peaks that are shifted during the charge-discharge process, as shown in *in-situ* XRD of the initial two cycles 2D view at 100 mA $g^{-1}$. Therefore, based on the CV and *in/ex-situ* XRD of SIB possible reaction mechanism equation can be expressed as follows.

### 3.5.3. Discharge process

$$Fe_3V_3O_8 + xNa^+ + xe^- \rightarrow Na_xFe_3V_3O_8 \tag{9}$$

$$Na_xFe_3V_3O_8 + yNa^+ + ye^- \rightarrow 3Fe + Na_{x+y}V_3O_8 \tag{10}$$

### 3.5.4. Charge process

$$Na_xFe_3V_3O_8 \rightarrow Na + Fe_3V_3O_8 \tag{11}$$

$$3Fe + Na_{x+y}V_3O_8 \rightarrow Na + Na_xFe_3V_3O_8 \tag{12}$$

Based on the sodium ion storage discharge capacity of 805 mA h $g^{-1}$ and equations 9–12, the electron transfer is possibly 16 and the theoretical capacity is 956.44 mA h $g^{-1}$ ($Fe_3V_3O_8$, $M_w = 448.35$ g $mol^{-1}$) can be confirmed. The intercalation reaction contributes more efficiently than the conversion reaction. The reduction in theoretical capacity can be attributed to the formation of a thick SEI layer on the electrode surface during the initial activation cycles. The activation cycles after promoting the diffusion of sodium ions into the FVO and the existence of the porous nature also aid the more active sites for the sodium-ion intercalation/de-intercalation process. Therefore, the specific cyclic capacity and rate performance exhibited more stability after the activation cycles. Overall, the reaction mechanism of bimetallic oxide-based materials through atomic or surface-level modification for high-capacity storage electrodes is highly anticipated for future high-energy density battery applications.

## 4. Conclusions

In summary, $Fe_3V_3O_8$ (FVO) was successfully synthesized via a facile hydrothermal method followed by a calcination process and used as a

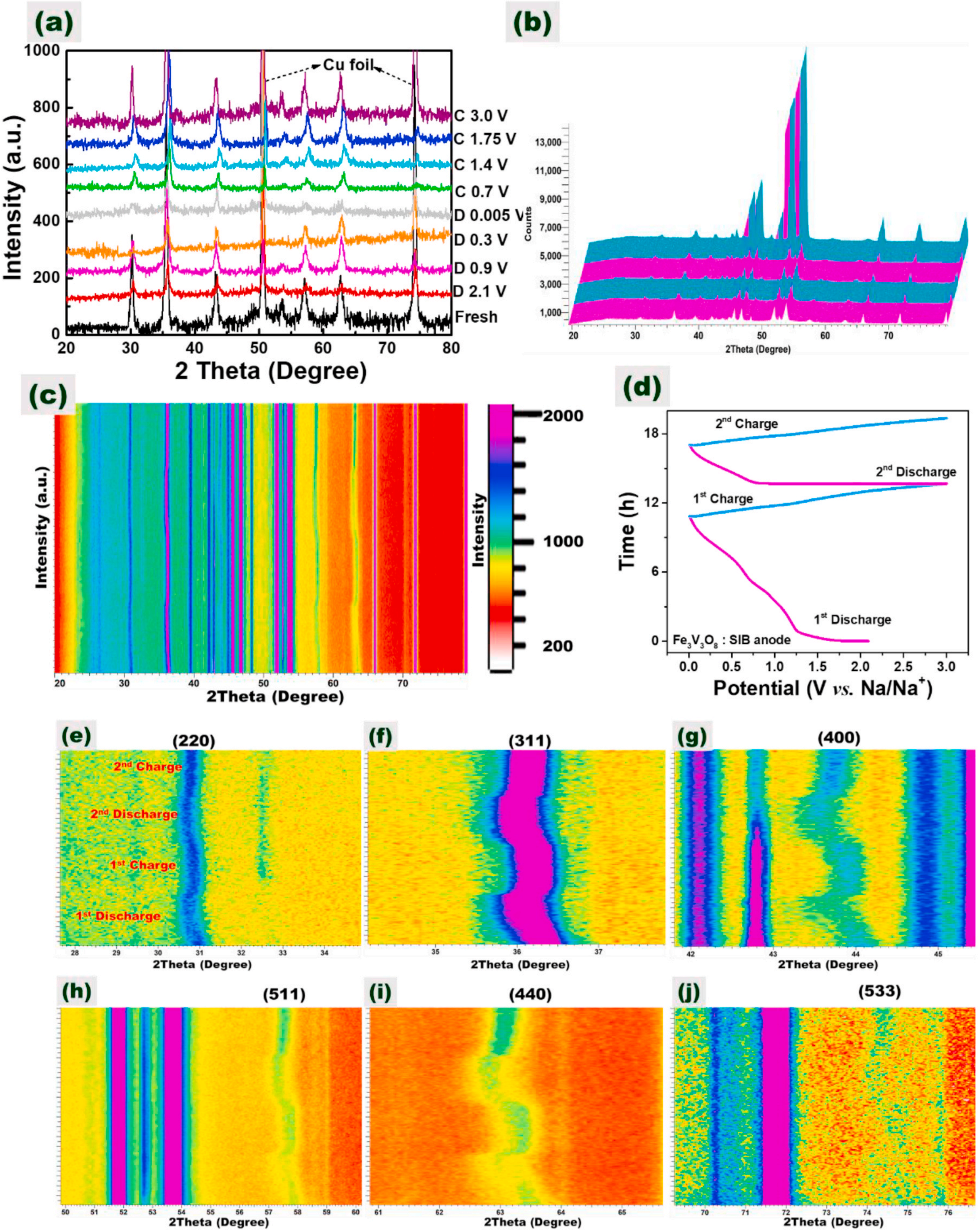

**Fig. 8.** Sodium-ion storage mechanism analysis: **(a)** *ex-situ* XRD of the first cycle at different potential points, **(b)** *in-situ* XRD patterns, **(c)** Contour plots of *in-situ* XRD, **(d)** the discharge-charge profiles of initial two cycles at 100 mA $g^{-1}$ for the *in-situ* XRD test (CC mode) and **(e–j)** the enlargement of the contour plots *in-situ* XRD FVO planes regions, respectively.

novel anode material for sodium-ion storage. The cubic crystalline pure phase structure without impurity phases was confirmed. The $Fe_3V_3O_8$ negative electrode for sodium-ion storage delivered a high reversible discharge capacity of 408 mA h $g^{-1}$ at a current density of 100 mA $g^{-1}$ and preserved 540 mA h $g^{-1}$ at 500 mA $g^{-1}$ over 200 cycles. The reversible discharge capacities of 419 and 253 mA h $g^{-1}$ were achieved at increased current densities of 500 and 1500 mA $g^{-1}$, respectively. Moreover, in long-term cycling at a current density of 2000 mA $g^{-1}$, a discharge capacity of 150 mA h $g^{-1}$ was maintained with 100 % of Coulombic efficiency over 1000 cycles. In addition, the lithium-ion storage capability was also predicted and the results showed better storage performance. Finally, the possible electrochemical reaction mechanisms were proposed in detail. The dual combination reaction mechanism was confirmed by ex-situ/in-situ XRD and CV analyses. The findings demonstrate that $Fe_3V_3O_8$ will be a promising potential anode material for high-performance sodium-ion and lithium-ion batteries.

Thus, the novel material with high-capacity and economical manufacturing will promote cost-effective, high-performance large-scale battery construction in future energy storage applications.

## CRediT authorship contribution statement

**Rasu Muruganantham:** Writing – original draft. **Jun-Ying Huang:** Methodology, Formal analysis. **Pei-Jun Wu:** Formal analysis. **Liang-Yin Kuo:** Writing – review & editing, Formal analysis. **Chun-Chuen Yang:** Formal analysis. **Yan-Gu Lin:** Formal analysis. **Ju Li:** Writing – review & editing. **Wei-Ren Liu:** Writing – review & editing, Supervision.

## Declaration of competing interest

The authors declare that they have no known competing financial interests or personal relationships that could have appeared to influence the work reported in this paper.

## Data availability

No data was used for the research described in the article.

## Acknowledgements

The authors wish to express their gratitude for the support provided by the National Science and Technology Council (NSTC) through project grants numbered NSTC 111-2622-E-033-007, 111-2811-E-033-001-MY3, 111-2221-E-033 -004 -MY3, 111-2923-E-006-009, 111-3116-F-011-005, NSTC 111-2222-E-131-002, 112-2218-E-007-023, 112-2923-E-006-004 and 112-2622-E-033-013. L.-Y. Kuo thanks the Ministry of Education of Taiwan through the Sustainable Electrochemical Energy Development Center (SEED), part of the Featured Areas Research Center Program. Computing time was granted through the National Center for High-performance Computing (NCHC) on Taiwania 3 in Hsinchu, Taiwan.

## Appendix A. Supplementary data

Supplementary data to this article can be found online at https://doi.org/10.1016/j.jpowsour.2024.234947.

## References

[1] J. Liu, J. Xiao, J. Yang, W. Wang, Y. Shao, P. Liu, M.S. Whittingham, The TWh challenge: next generation batteries for energy storage and electric vehicles, Next Energy 1 (2023) 100015.

[2] C. Chen, Y. Lu, Y. Ge, J. Zhu, H. Jiang, Y. Li, Y. Hu, X. Zhang, Synthesis of nitrogen-doped electrospun carbon nanofibers as anode material for high-performance sodium-ion batteries, Energy Technol. 4 (2016) 1440–1449.

[3] L. Xu, P. Xiong, L. Zeng, Y. Fang, R. Liu, J. Liu, F. Luo, Q. Chen, M. Wei, Q. Qian, Electrospun $VSe_{1.5}$/CNF composite with excellent performance for alkali metal ion batteries, Nanoscale 11 (2019) 16308–16316.

[4] C. Vaalma, D. Buchholz, M. Weil, S. Passerini, A cost and resource analysis of sodium-ion batteries, Nat. Rev. Mater. 3 (2018) 1–11.

[5] S. Fang, D. Bresser, S. Passerini, Transition metal oxide anodes for electrochemical energy storage in lithium-and sodium-ion batteries, Adv. Energy Mater. 10 (2020) 1902485.

[6] Y. Li, Y. Lu, C. Zhao, Y.-S. Hu, M.-M. Titirici, H. Li, X. Huang, L. Chen, Recent advances of electrode materials for low-cost sodium-ion batteries towards practical application for grid energy storage, Energy Storage Mater. 7 (2017) 130–151.

[7] R. Muruganantham, Y.-J. Gu, Y.-D. Song, C.-W. Kung, W.-R. Liu, Ce-MOF derived ceria: insights into the Na-ion storage mechanism as a high-rate performance anode material, Appl. Mater. Today 22 (2021) 100935.

[8] S. Cheng, Q. Ru, Z. Shi, Y. Gao, Y. Liu, X. Hou, F. Chen, F.C.-C. Ling, Plant oil–inspired 3D flower-like $Zn_3V_3O_8$ nanospheres coupled with N-doped carbon as anode material for Li-/Na-ion batteries, Energy Technol. 7 (2019) 1900754.

[9] X. Deng, Z. Chen, Y. Cao, Transition metal oxides based on conversion reaction for sodium-ion battery anodes, Mater. Today Chem. 9 (2018) 114–132.

[10] S. Wang, C. Sun, N. Wang, Q. Zhang, Ni-and/or Mn-based layered transition metal oxides as cathode materials for sodium ion batteries: status, challenges and countermeasures, J. Mater. Chem. A 7 (2019) 10138–10158.

[11] Y. Sun, S. Guo, H. Zhou, Adverse effects of interlayer-gliding in layered transition-metal oxides on electrochemical sodium-ion storage, Energy Environ. Sci. 12 (2019) 825–840.

[12] S. Boyd, V. Augustyn, Transition metal oxides for aqueous sodium-ion electrochemical energy storage, Inorg. Chem. Front. 5 (2018) 999–1015.

[13] Q. Liu, Z. Hu, M. Chen, C. Zou, H. Jin, S. Wang, S.L. Chou, Y. Liu, S.X. Dou, The cathode choice for commercialization of sodium-ion batteries: layered transition metal oxides versus Prussian blue analogs, Adv. Funct. Mater. 30 (2020) 1909530.

[14] C. Feng, L. Li, Z. Guo, C. Zhang, J. Wang, S. Wang, Synthesis and electrochemical properties of $VO_x$/C nanofiber composite for lithium ion battery application, Mater. Lett. 117 (2014) 134–137.

[15] J. Zhang, Q. Li, Z. Liao, L. Wang, J. Xu, X. Ren, B. Gao, P.K. Chu, K. Huo, In situ synthesis of $V_2O_3$-intercalated N-doped graphene nanobelts from $VO_x$-amine hybrid as high-performance anode material for alkali-ion batteries, Chemelectrochem 5 (2018) 1387–1393.

[16] X. Zhou, X. Chen, Q. Bi, X. Luo, L. Sun, Z. Liu, A scalable strategy to synthesize $TiO_2$-$V_2O_5$ nanorods as high performance cathode for lithium ion batteries from $VO_x$ quasi-aerogel and tetrabutyl titanate, Ceram. Int. 43 (2017) 12689–12697.

[17] J. Wang, C. Cui, G. Gao, X. Zhou, J. Wu, H. Yang, Q. Li, G. Wu, A new method to prepare vanadium oxide nano-urchins as a cathode for lithium ion batteries, RSC Adv. 5 (2015) 47522–47528.

[18] M. Zhen, L. Liu, C. Wang, Ultrathin mesoporous $ZnCo_2O_4$ nanosheets as anode materials for high-performance lithium-ion batteries, Microporous Mesoporous Mater. 246 (2017) 130–136.

[19] F. Xu, F. Yu, C. Liu, P. Han, B. Weng, Hierarchical carbon cloth supported $Li_4Ti_5O_{12}$@ $NiCo_2O_4$ branched nanowire arrays as novel anode for flexible lithium-ion batteries, J. Power Sources 354 (2017) 85–91.

[20] L. Zhang, Q. Tang, X. Chen, B. Fan, K. Xiao, S. Zhang, W. Deng, A. Hu, Self-assembled synthesis of diamond-like $MnCo_2O_4$ as anode active material for lithium-ion batteries with high cycling stability, J Alloy Compd 722 (2017) 387–393.

[21] H. Shin, W.-J. Lee, Multi-shelled $MgCo_2O_4$ hollow microspheres as anodes for lithium ion batteries, J. Mater. Chem. A 4 (2016) 12263–12272.

[22] M. Silambarasan, P. Ramesh, D. Geetha, V. Venkatachalam, A report on 1D $MgCo_2O_4$ with enhanced structural, morphological and electrochemical properties, J. Mater. Sci. Mater. Electron. 28 (2017) 6880–6888.

[23] D. Cai, B. Qu, Q. Li, H. Zhan, T. Wang, Reduced graphene oxide uniformly anchored with ultrafine $CoMn_2O_4$ nanoparticles as advance anode materials for lithium and sodium storage, J Alloy Compd 716 (2017) 30–36.

[24] C. Zhu, Z. Liu, J. Wang, J. Pu, W. Wu, Q. Zhou, H. Zhang, Novel $Co_2VO_4$ anodes using ultralight 3D metallic current collector and carbon sandwiched structures for high-performance Li-ion batteries, Small 13 (2017) 1701260.

[25] Y.-Y. Huang, L.-Y. Lin, Synthesis of ternary metal oxides for battery-supercapacitor hybrid devices: influences of metal species on redox reaction and electrical conductivity, ACS Appl. Energy Mater. 1 (2018) 2979–2990.

[26] H.-Y. Sun, L.-Y. Lin, Y.-Y. Huang, W.-L. Hong, Nickel precursor-free synthesis of nickel cobalt-based ternary metal oxides for asymmetric supercapacitors, Electrochim. Acta 281 (2018) 692–699.

[27] L.-Y. Lin, X. Li, Y.-Y. Huang, H.-Y. Sun, Synthesizing Ni-based ternary metal compounds for battery-supercapacitor hybrid devices with and without using nickel precursors, Mater. Sci. Semicond. Process. 98 (2019) 81–89.

[28] S. Zhang, H. Tan, X. Rui, Y. Yu, Vanadium-based materials: next generation electrodes powering the battery revolution? Accounts of Chemical Research 53 (2020) 1660–1671.

[29] F. Wu, S. Xiong, Y. Qian, S.-H. Yu, Hydrothermal synthesis of unique hollow hexagonal prismatic pencils of $Co_3V_2O_8 \cdot n\ H_2O$: a new anode material for lithium-ion batteries, Angew. Chem. Int. Ed. 54 (2015) 10787–10791.

[30] H. Ma, S. Zhang, W. Ji, Z. Tao, J. Chen, $\alpha$-$CuV_2O_6$ nanowires: hydrothermal synthesis and primary lithium battery application, J. Am. Chem. Soc. 130 (2008) 5361–5367.

[31] V. Soundharrajan, B. Sambandam, J. Song, S. Kim, J. Jo, S. Kim, S. Lee, V. Mathew, J. Kim, $Co_3V_2O_8$ sponge network morphology derived from metal–organic framework as an excellent lithium storage anode material, ACS Appl. Mater. Interfaces 8 (2016) 8546–8553.

[32] M. Li, Y. Gao, N. Chen, X. Meng, C. Wang, Y. Zhang, D. Zhang, Y. Wei, F. Du, G. Chen, $Cu_3V_2O_8$ nanoparticles as intercalation-type anode material for lithium-ion batteries, Chem. Eur J. 22 (2016) 11405–11412.

[33] C. Wang, D. Fang, H.e. Wang, Y. Cao, W. Xu, X. Liu, Z. Luo, G. Li, M. Jiang, C. Xiong, Uniform nickel vanadate ($Ni_3V_2O_8$) nanowire arrays organized by ultrathin nanosheets with enhanced lithium storage properties, Sci. Rep. 6 (2016) 20826.

[34] Y. Jin, J. He, Z. Ou, C. Feng, G. Zhang, Synthesis and electrochemical properties of $Zn_3V_3O_8$ as novel anode material, Chin. Chem. Lett. 30 (2019) 806–808.

[35] R. Nie, G. Fang, J. Zhou, J. Guo, Y. Tang, S. Liu, Y. Cai, P. Hao, S. Liang, Three-dimensional $Zn_3V_3O_8$/carbon fiber cloth composites as binder-free anode for lithium-ion batteries, Electrochim. Acta 246 (2017) 97–105.

[36] H. Xue, Y. Fang, L. Zeng, X. He, F. Luo, R. Liu, J. Liu, Q. Chen, M. Wei, Q. Qian, Facile synthesis of hierarchical lychee-like $Zn_3V_3O_8$@C/rGO nanospheres as high-performance anodes for lithium ion batteries, J. Colloid Interface Sci. 533 (2019) 627–635.

[37] C. Bie, J. Pei, G. Chen, Q. Zhang, J. Sun, Y. Yu, D. Chen, Hierarchical $Zn_3V_3O_8$/C composite microspheres assembled from unique porous hollow nanoplates with superior lithium storage capability, J. Mater. Chem. A 4 (2016) 17063–17072.

[38] J. Liu, P. Zhang, W. Wang, C. Zhou, J. Zhou, J. Wu, K. Li, Y. Lei, L. Chen, $Zn_3V_3O_8$/NC hybrid microspheres self-assembled by layered porous nanosheets as a superior

anode material for lithium/sodium-ion batteries, Dalton Trans. 50 (2021) 4017–4027.

[39] Y. Bai, Y. Tang, Y. Gao, X. Li, L. Liu, Y. Zhang, S. Gao, Bamboo-like porous CNTs encapsulated $Zn_3V_3O_8$ nanoparticles as high-performance anodes for lithium ion batteries, J Alloy Compd 798 (2019) 678–684.

[40] T. Li, M. Lu, Y. Zhang, X. Xiang, S. Liu, C. Chen, Structural evolution and redox chemistry of robust ternary layered oxide cathode for sodium-ion batteries, J Alloy Compd 978 (2024) 173459.

[41] Z. Zhang, j. Zhou, X. Zhou, C. Wang, Z. Pan, X. Xu, X. Liu, Z. Wang, Y. Wu, S. Jiang, Y. Zhang, Graphene oxide-supported $MnV_2O_6$ nanoribbons with enhanced electrochemical performance for sodium-ion batteries, J. Power Sources 597 (2024) 234117.

[42] M. Ghodrati, M. Mousavi-Kamazani, S. Zinatloo-Ajabshir, $Zn_3V_3O_8$ nanostructures: facile hydrothermal/solvothermal synthesis, characterization, and electrochemical hydrogen storage, Ceram. Int. 46 (2020) 28894–28902.

[43] B. Suganya, S. Maruthamuthu, J. Chandrasekaran, B. Saravanakumar, E. Vijayakumar, R. Marnadu, H.E. Ali, T.D. Nguyen, Nitrogen doped 2D graphene/$Zn_3V_2O_8$ nanocomposite with enhanced supercapacitive features, Surface. Interfac. 24 (2021) 101129.

[44] T. Liu, Y. Liu, C. Niu, Z. Chao, Pseudocapacitive contribution in amorphous $FeVO_4$ cathode for lithium-ion batteries, Chemelectrochem 9 (2022) e202101493.

[45] X. Li, J. Zhang, Y. Zhang, B. Zhang, H. Liu, Q. Xu, Y. Xia, A facile Ball-Milling preparation strategy of Nitrogen-Doped carbon coated $Na_4Fe_3(PO_4)_2P_2O_7$ Nano-Flakes with superior sodium ion storage performance, Chem. Eng. Sci. 260 (2022) 117951.

[46] H. Chai, Y. Wang, Y. Fang, Y. Lv, H. Dong, D. Jia, W. Zhou, Low-cost synthesis of hierarchical $Co_3V_2O_8$ microspheres as high-performance anode materials for lithium-ion batteries, Chem. Eng. J. 326 (2017) 587–593.

[47] Y. Sun, C.-S. Li, Q.-R. Yang, S.-L. Chou, H.-K. Liu, Electrochemically active, novel layered m-$ZnV_2O_6$ nanobelts for highly rechargeable Na-ion energy storage, Electrochim. Acta 205 (2016) 62–69.

[48] K.-H. Kim, S.-H. Hong, Investigation of sodium storage in manganese vanadate $MnV_2O_6$ nanobelt and nanoparticle as an anode for sodium-ion batteries, Electrochim. Acta 367 (2021) 137520.

[49] A.K. Kakarla, D. Narsimulu, H. Bandi, R. Shanthappa, J.S. Yu, Facile synthesis of N-doped reduced graphene oxide matrix-covered porous $Fe_2VO_4$ hybrid composite nanostructures as anode material for lithium-ion batteries, J Alloy Compd 960 (2023) 170784.

[50] D. Zhao, Z. Zhang, J. Ren, Y. Xu, X. Xu, J. Zhou, F. Gao, H. Tang, S. Liu, Z. Wang, D. Wang, Y. Wu, X. Liu, Y. Zhang, $Fe_2VO_4$ nanoparticles on rGO as anode material for high-rate and durable lithium and sodium ion batteries, Chem. Eng. J. 451 (2023) 138882.

[51] H. Xu, J. Fan, D. Pang, Y. Zheng, G. Chen, F. Du, Y. Gogotsi, Y. Dall'Agnese, Y. Gao, Synergy of ferric vanadate and MXene for high performance Li- and Na-ion batteries, Chem. Eng. J. 436 (2022) 135012.

[52] X. Ding, X. Huang, J. Jin, H. Ming, L. Wang, J. Ming, Advanced and safer lithium-ion battery based on sustainable electrodes, J. Power Sources 379 (2018) 53–59.

[53] B. Sambandam, V. Soundharrajan, J. Song, S. Kim, J. Jo, D.T. Pham, S. Kim, V. Mathew, K.H. Kim, Y.-K. Sun, J. Kim, $Ni_3V_2O_8$ nanoparticles as an excellent anode material for high-energy lithium-ion batteries, J. Electroanal. Chem. 810 (2018) 34–40.

[54] Q. Zhang, J. Pei, G. Chen, C. Bie, D. Chen, Y. Jiao, J. Rao, $Co_3V_2O_8$ hexagonal pyramid with tunable inner structure as high performance anode materials for lithium ion battery, Electrochim. Acta 238 (2017) 227–236.

[55] V. Soundharrajan, B. Sambandam, J. Song, S. Kim, J. Jo, D.T. Pham, S. Kim, V. Mathew, J. Kim, Bitter gourd-shaped $Ni_3V_2O_8$ anode developed by a one-pot metal-organic framework-combustion technique for advanced Li-ion batteries, Ceram. Int. 43 (2017) 13224–13232.

[56] J. Tang, S. Ni, B. Zhou, D. Chao, T. Li, X. Yang, Theoretical calculation and experimental verification of $Zn_3V_3O_8$ as an insertion type anode for LIBs, J. Alloys Compd. 730 (2018) 228–233.

[57] R. Jin, R. Li, H. Xu, Gram-scale synthesis of F-doped $Ni_3V_2O_8$ nanorods with high initial Coulombic efficiency as anode for lithium ion batteries, Ceram. Int. 47 (2021) 24625–24631.

[58] Q. An, F. Lv, Q. Liu, C. Han, K. Zhao, J. Sheng, Q. Wei, M. Yan, L. Mai, Amorphous vanadium oxide matrixes supporting hierarchical porous $Fe_3O_4$/graphene nanowires as a high-rate lithium storage anode, Nano Lett. 14 (2014) 6250–6256.

[59] Y. Chen, X.-F. Zhang, A.-J. Wang, Q.-L. Zhang, H. Huang, J.-J. Feng, Ultrafine $Fe_3C$ nanoparticles embedded in N-doped graphitic carbon sheets for simultaneous determination of ascorbic acid, dopamine, uric acid and xanthine, Microchim. Acta 186 (2019) 660.

[60] J. Zheng, K. Liang, K. Shi, Y. Qiu, In situ synthesis and electrochemical properties of Fe/$Li_2O$ as a high-capacity cathode prelithiation additive for lithium ion batteries, Int. J. Electrochem. Sci. 14 (2019) 5305–5316.

[61] T.S. Attaa, A.N. Abd, M.J. Zoory, A comparative study of the photoelectric properties for lithium oxide prepared by Green synthesis method, J. Phys. Conf. 1963 (2021) 012148.

[62] B. Sridhar, S.V.S. Prasad, K. Dasari, E. Parthiban, Structural properties of lithium doped V3O8 nanorods synthesized by hydrothermal method, Mater. Today: Proc. (2023).

[63] N. Zhang, X. Han, Y. Liu, X. Hu, Q. Zhao, J. Chen, 3D porous γ-$Fe_2O_3$@C nanocomposite as high-performance anode material of Na-ion batteries, Adv. Energy Mater. 5 (2015) 1401123.